RSC Advances

ROYAL SOCIETY
OF CHEMISTRY

www.rsc.org/advances

Journal Name

ARTICLE TYPE

A 3D hierarchical honeycomb structured MWCNTs coupled with CoMnAl-LDO: fabrication and application for ultrafast catalytic degradation of bisphenol A

Wen Li,[a] **Pingxiao Wu,**[*,a,b] **Shanshan Yang**[a]**, Yajie Zhu,**[a] **Chunxi Kang,**[a] **Ly Tuong Tran,**[a] **Beilei Zeng,**[a]

A 3D hierarchical honeycomb nano-structured o-MWCNTs coupled with CoMnAl-layer double oxides has been successfully fabricated and characterized as a heterogeneous catalyst for bisphenol A (BPA) degradation using potassium monopersulfate (PMS) as oxidant. The role of MWCNTs was investigated
10 and discussed in terms of surface morphology, structure, composition and catalytic activity of the as-prepared nanohybrid by investigation of SEM, TEM, XRD, XPS, Ranman et al.. The results showed that catalytic performance of the CNTs-LDO can be significantly enhanced with the increase of o-MWCNTs contents in the hybrids, and MWCNTs provided an orientation/confinement for nanohybrid formation and the defect generated by calcination might increase PMS activation for the production of sulfate radicals.

1. Introduction

Carbon nanomaterials, including carbon nanotubes (CNTs), graphene and fullerene, are a kind of novel nanomaterials with a monolayer of carbon atoms arranged in a honeycomb lattice. The fascinating properties of the carbon nanomaterials, such as unique
20 electronic property, large surface area, high chemical and thermal stability, and excellent mechanical flexibility have been well documented [1].Very recently, carbon nanomaterials have been arousing enormous interests among the researchers in the application of catalytic degradation of pollutants [2-4]. Previous
25 study [5], in our laboratory found that a trace level of reduced graphene oxide was able to significantly facilitate the degradation of cationic dye methylene blue and anionic dye orange G in aqueous solutions, and both the sp[2]-hybridized carbon and that zigzag carbons played important roles in the photocatalysis
30 process. It also showed that carbon nanomaterials or functional carbon nanomaterials can promote decomposition of oxidants (e.g., H_2O_2, PMS, PDS) into radicals, thereby enhancing the oxidation of organic compounds in liquids[6-9].

To improve the hydrophilicity and catalytic activity of the
35 carbon nanomaterials, an array of surface functional groups, such as hydroxyl, carboxyl, and amino groups are often introduced to functionalize these materials. Owing to case of acidity or basicity possessed by that many of these surface functional groups, carbon nanomaterials exerted potential in degradation of organic
40 contaminants by acid-catalyzed and base-catalyzed in the nucleophilic and hydrolytic reactions [10]. In addition, defects which formed inevitably during the modification or functionalization can increase the proportion of adsorbed oxygen species onto the surface lattice oxygen ones and thus improve the
45 catalytic activity[11, 12]. What's more, the oxygen functional surface species, such as ketonic (C=O) group, are rich in electrons and thus have great potential to coordinate a redox process [13]. Based on the abovementioned analysis, sp[2]-hybridized carbon, surface acidity/basicity, lattice defects and oxygen-containing functional
50 groups are deemed to be the origins of the catalytic activity.

The construction of hierarchical structures by arranging carbon nanomaterials and metal oxide nanoparticles with nanometer-scale precision exhibits a superior prospect in the application of nanotechnology [14]. Therefore, it inspired us to
55 prepare a novel kind of composite materials with morphology, structure, composition and properties which are different from those of the simple sum of the individual parts. Particularly, the combination of metal oxides and carbon nanomaterials endows the composites with the unique properties of each component or
60 even with a synergistic effect when apply them in the heterogeneous catalysis. For example, the CNTs network was found to be effective in facilitating the dispersion of the oxide nanoparticles and providing exposure of more active sites outside because of their large surface areas and interaction between the
65 functional groups and meta ions [5, 15]. Moreover, surface sites may be classified as the delocalized π electrons on the graphene layers (C-π), which provide continuous conducting pathways for the electrons transportation and thus accelerate the reactions [5, 15]. Besides, the morphology, structure and composition of metal
70 oxides could be affected by the introduction of CNTs; e.g., Song[16] prepared VO_2 supported on multi-walled carbon nanotube (MWCNTs) by the spontaneous redox between V^{5+} and the defects of MWCNTs, the resulting catalysts had a better catalytic performance than V_2O_5 loaded directly on MWCNTs; Dang [17]
75 synthesized crystalline hollow manganese oxide nanotubes with highly porous walls using CNTs as templates and they found that this kind of material exhibited excellent catalytic performances on the degradation of organic dye. Consequently, it seems necessary to study of the interaction between CNTs and metal

oxides and the application of the hybrid materials.

In view of those above mentioned reasons, composites of CNTs with catalytic metal oxides or metal hydroxides have been the subject of many studies[18-20]. Among various metal elements, the group VII metals, especially the iron-group-metal Fe, Mn and Co, exhibit promising catalysis activity in heterogeneous reactions [21-23]. The iron-group-metal-based catalysts have attracted enormous interests as low-cost alternatives to noble-metal catalysts. Layered double hydroxides (LDHs) are a family of common inorganic materials and are easily synthesized in the laboratory. A key structural characteristic of LDHs is that the M^{II} and M^{III} cations distributed in a uniform manner in the hydroxide layers[24]. Therefore, it can be used as precursor or template for fabricating catalyst with specific/morphology/surface structure and high dispersion by lattice orientation/lattice confinement of LDHs [25].

In this study, we describe an approach of fabricating MWCNTs coupled with layers of CoMnAl mixture metal oxides with 3D hierarchical honeycomb nano-structure and investigate its catalytic performance in potassium monopersulfate (PMS) oxidation of bisphenol A (BPA). Particular attention was paid to the changes of morphology, structure and composition of the hybrids in the absence and presence of MWCNTs. The stability and recycle of the catalysts, as well as the catalysis mechanism were also studied.

2.   Materials and methods

2.1.   Synthesis of Catalysts.

Commercial MWCNTs were purchased form Nanjing XFNANO Materials Tech Co., Ltd, China. The MWCNTs have a outer diameter of < 8nm and inner diameter of 2-5 nm, a length of 0.5-2 μm, and a purity of > 95% by weight. Pristine MWCNTs were treated with a mixture of nitric acid and sulfuric acid (in a volume ration of 1:3) aqueous solution by refluxing in a round-bottom flask at 100℃ for 4h, and then filtered and washed with distilled water to neutrality. Finally, the collected power was dried at 80 ℃ for 12 h in an oven to obtain the modified MWCNTs that are denoted as o-MWCNTs.

CNT-LDH nanohybrids were fabricated via a homogeneous urea precipitation method. For a typical run, a certain amount of $Co(NO_3)_2 \cdot 6H_2O$, $Mn(NO_3)_2$, $Al(NO_3)_2 \cdot 9H_2O$ (the metal ion molar ration is 4:1:1) and urea were dissolved in 500 ml of distilled water to obtain the mixed solution by ultrasonication for 10 min. Then, 50 mg of o-MWCNTs were dispersed in the above mixed solutions and ultrasonicated for 4h. According to the total metal contents added into the mixed solution, the nanohybrids were denoted as CNTs-LDH-X, where X represented the mass ratio of CNTs to LDH. In this work, four samples with different ratios (CNTs-LDH-0.06, CNTs-LDH-0.31, CNTs-LDH-0.62 and CNTs-LDH-1.23) were prepared for investigating the effect of CNTs on the catalytic activity. The mixture was transferred into a three-necked round-bottom flask after standing and adsorption for overnight. Subsequently, the mixed solution was refluxed for 48 h. After filtering and washing with distilled water several times, the resulting precipitant was drided at 60℃ in vacuum overnight, yielding the final CNTs-LDH nanohybrids. The dried products were calcined for 5 h

at 400℃ and denoted as CNTs-LDO-0.06, CNTs-LDO-0.31, CNTs-LDO-0.62 and CNTs-LDO-1.23, respectively. For comparison, the pristine LDO was prepared under the same conditions except for the addition of o-MWCNTs.

2.2 Characterization

Thermogravimetry-differential scanning calorimetry (TG-DSC) date were obtained by using a thermal analysis meter (STA-449F3, Netasch, Germany) under air environment with a heating rate of 10°C·min⁻¹. The erternal surface microstructure of the samples'external surface was observed by a ZEISS Merlin Scanning electron microscopy (SEM, Carl Zeiss, Germany) and a high resolution transmission electron microscopy (TEM, JEM-3010, JEOL Ltd., Japan) with an accelerating voltage of 200 kV. The X-ray diffraction (XRD) patterns were measured by a X-ray diffractometer equipped (D/MAX-ⅢA, Rigaku Ltd., Japan) with Cu Kα radiation. The particle surface area and pore size measurement were carried out by N_2 adsorption/desorption isotherm analysis with a Chemi-sorption Surface Area Analyzer (ASAP 2010, Micrometritics, America). The X-ray photoelectron spectra (XPS) were measured with an X-ray photoelectron spectrometer (AES430S, ANELVA, Japan) and the binding energy of C 1S was shifted to 284.6 eV as an internal reference.

Cyclic voltammetry (CV) tests were performed at 25℃ in a three-electrode cell connected to a AUTOLAB PGSTAT302N workstation (AUT83939, ECO CHEMIE BV, Netherlands). The working electrode was a glassy carbon disk (GC) with an area of 0.071 cm² and coated with catalysts to form the catalysts layer. Ag/AgCl and a platinum foil served as reference and counter electrodes, respectively. The catalysts ink for GC was prepared by blending 2 mg catalyst, 2 mL ethanol and 10 μL Nafion emulsion, which was ultrasonically dispersed for 10 min to form suspension. Then, 10 μL of this suspension was deposited onto the surface GC pipette, and then dried at room temperature. Electrochemical experiments were carried out in O_2-saturated B-R buffer solution with pH = 3 at room temperature. CVs were initially collected by scanning the disk potential from -0.4 V to 0.6 V at a scan rate of 10 mV·s⁻¹ to measure the surface behavior of the catalysts.

2.3. Catalytic activity test

The degradation of BPA was carried out at 25 °C in a 1 L glass vessel with 500 mL of BPA solution at 10-40 mg·L⁻¹ with a constant stirring. The reactor was attached to a stand and dipped into a water bath. First, 0.01 g catalysts was added into the BPA solution for a while, then the PMS ($2KHSO_5 \cdot KHSO_4 \cdot K_2SO_4$, Aladdin) was added into the solution at 0.15 g·L⁻¹. It must be noted that PMS addition in unbuffered water would lead to a significant decrease in the pH. Therefore, phosphate buffer solution was used to maintain the neutral condition (pH = 7.0) of the solution. At predetermined time internals, the samples (1 mL) were withdrawn by syringe and filtered by 0.45 μm PES (polyethersulfone) membranes. The BPA concentrations in filtered solutions were then quantified by high performance liquid chromatography (HPLC, Hitachi, L-2000) with an HP UV detector at 276 nm. A Synergi 4u Polar-RP 80 column (diameter, 250×4.60 mm) and a guard column (diameter, 4.6×12 mm) were used. Mobile phase was consisted of water and acetonitrile

(50:50) at 1.0 mL·min^{-1}.

To evaluate the stability of the catalysts, the leaching amounts of cobalt and manganese after reaction were measured by zeeman atomic absorption spectrometry (AAS, Z-2000, Hitachi).

For the recycle tests, the catalysts were recovered by filtration, thoroughly washed with distilled water for several times, then dried at 60 ^{o}C overnight after each run. The catalyst losses were observed during the recycle processes. Therefore, several parallel reactions were conducted in the first and second runs to ensure a sufficient amount of catalysts for the next run.

3. Results

3.1. Catalyst characterization

3.1.1 TG analysis

The thermal behaviors of the o-MWCNTs in air were examined by TG-DSC analysis. As can be seen in Fig. 1, the weight loss of o-MWCNTs occurs primarily in two steps: the first one (10 wt%) at low temperature (ca. 30-450 ^{o}C) corresponds to the removal of adsorbed water, disintegration of amorphous carbon impurities or the dehydroxylation and decarboxylation; the second one which presents significant weight losses (90 wt%) at the temperature range of ca. 450-725 ^{o}C may be due to the decomposition of CNTs. The combustion point of CNTs in the composites was found to be 450 ^{o}C because of the highest rate of mass loss at this point. Therefore, the loss of CNTs during the composite preparation procedure was negligible. The broad peak at 585 ^{o}C in DSC can be assigned to the burning of MWCNTs, while another peak at 701 ^{o}C indicates the combustion of the graphite residues[26].
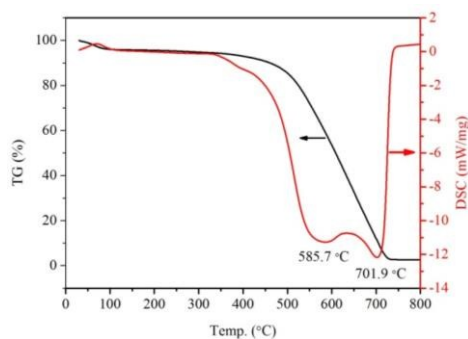

Fig. 1. TG-DSC curves of o-MWCNTs

3.1.2 SEM and TEM analysis

The SEM image (Fig.2 (a)) shows that CoMnAl-LDH sheets are around 1.8 μm in wideness and possess high crystallinity and a 2D hexagonal plate-like structure which is typical morphology for layered double hydroxide. The hexagonal morphology is evidenced by TEM images (Fig. 2 (c)), in which the gauze-like LDH sheets can be clearly observed. The representative TEM image of o-MWCNTs reveals an entangled network consisting of numerous individual nanotubes with less than 8 nm in diameter and length up to micrometer scale (Fig.S1(a)). The CNTs-LDH composites were prepared via an in situ growth procedure in which CoMnAl-LDH nanosheets self-assembled on the surface of o-MWCNTs to form a unique 3D hierarchical nano-structure (as shown in Fig.2 (b), (c) and (d)). However, the 2D hexagonal

LDH sheets are also found in the composites due to the excessive amounts of metal ions in solution. A top view of SEM image (as shown in Fig.2 (d)) reveals that the LDH nanosheets with around 8 nm in thickness are grafted throughout the longitudinal axis of the nanotubes (grow on the oxidative sites of o-MWCNTs and parallel to the axis of the o-MWCNTs) to form a new 2D nanosheets. These 2D nanosheets arrays then grow on the surface of LDH sheets with 1.8 μm in wideness (highlighted by the arrow in Fig.2 (b)), leading to an interesting 3D hierarchical honeycomb nano-structure. This resulting structure can efficiently avoid the stacking and aggregation of individual o-MWCNTs and LDH sheets. Such a 3D hierarchical honeycomb nano-structure with a perpendicular growth of CNTs-LDH nanosheets arrays on the surface of LDH is also confirmed by the TEM image (Fig. 2 (f)). As shown, on the left of the red line, the LDH substrate is 1-2 μm in wideness, on which CNTs-LDH nanosheets (black lines on the substrate) are distributed. Conversely, on the right of the red line, there are no black lines on the 2D hexagonal LDH sheets. It should be noted that, the composites after calcination (as shown in Fig. S1) retaine the 3D hierarchical honeycomb nano-structure even part of amorphous o-MWCNTs was decomposed.
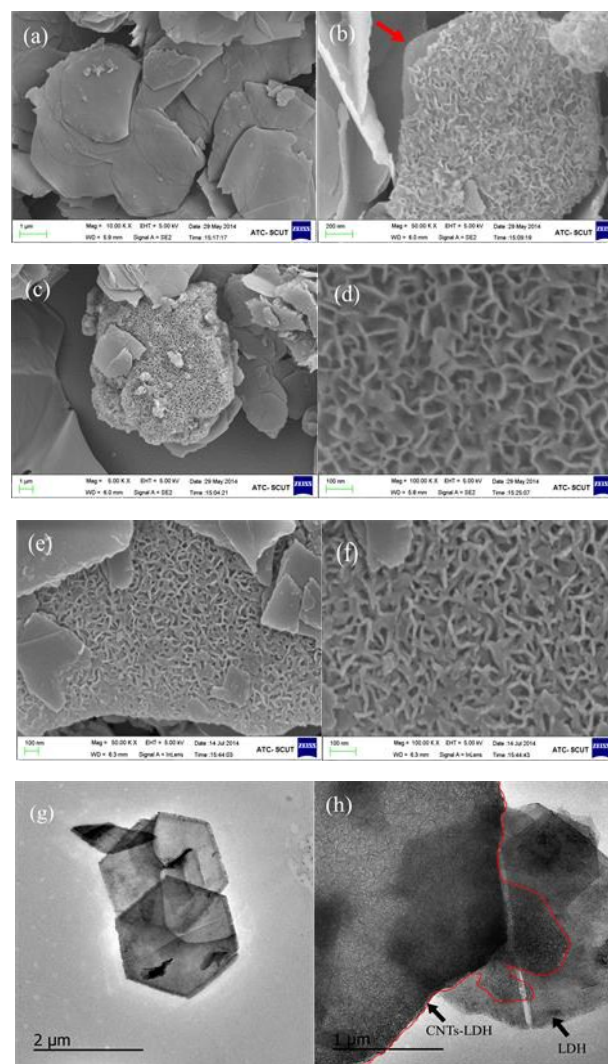

Fig. 2. SEM images of (a) LDH, (b) CNTs-LDH-0.62, (c) and (d) CNTs-LDH-1.23, (e) and (f) CNTs-LDO-1.23 and TEM images of (g) LDH and (h) CNTs-LDH-0.62.

ARTICLE TYPE

Table 1 The basal spacing (d_{003}), graphitization(I_D/I_G), BET surface area (S_{BET}), total pore volume (V_P) and average pore diameter (D_P) of samples.

Samples	d_{003} (Å)	I_D/I_G	Samples	I_D/I_G	S_{BET} (m² • g⁻¹)	V_Pᵃ(m² • g⁻¹)	D_P
o-MWCNTs	-	0.43	o-MWCNTs	-	432.96	0.45	4.37
LDH	7.63	-	LDO	-	141.13	0.15	5.71
CNTs-LDH-0.06	7.59	1.07	CNTs-LDO-0.06	-	146.87	0.17	5.88
CNTs-LDH-0.31	7.62	1.43	CNTs-LDO-0.31	1.71	162.09	0.24	7.91
CNTs-LDH-0.62	7.65	1.57	CNTs-LDO-0.62	1.83	173.95	0.26	7.72
CNTs-LDH-1.23	7.71	1.41	CNTs-LDO-1.23	0.68	206.48	0.37	8.50

ᵃ The total pore volume was evaluated for a P/P_0 ration of 0.97.

The chemical composition of the catalysts were analyzed using an energy dispersive spectrometer (EDS). The EDS results
5 (Fig. S2) show that the C concentration in the catalysts increased after adding o-MWCNTs. The carbon element also was detected in LDH and LDO, which suggests the CoMnAl-LDH is referred to CO_3-LDH.
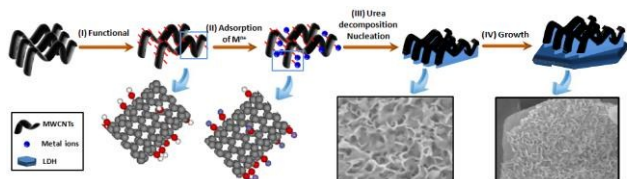
10 Scheme 1.Schematic illustration of the synthesis and morphology of CNTs-LDH. Step (I): the surface modification of MWCNTs by functional groups (e.g., -OH, -CO, -COOH). Step (II): the adsorption of Co^{2+}, Mn^{2+} and Al^{3+}. Step (III): the formation of 2D CNTs-LDH nanosheets by urea decomposition and nucleation. Step (IV): the formation of 3D hierarchical
15 honeycomb nano-structure by growing bigger LDH sheets substrate.

The concentration of metal ions in liquids before and after adding o-MWCNTs were detected by AAS respectively and the results are listed in Table S1. The concentration of metal ions slightly decreased after adsorption due to small amounts of
20 functional groups on the surface of MWCNTs. A possible formation and growth protocol is schematically shown in Scheme 1. A conventional acid treatment of CNTs introduced functional groups, e.g., hydroxyl and carbonyl groups (Scheme 1: Step I), which served as bonding sites for the adsorption of metal ions by
25 electrostatic forces (Scheme 1: Step II). These anchored metal ions acted as nucleation centers for the deposition of CoMnAl-LDH through a facile in situ growth method (Scheme 1: step III). Then CoMnAl-LDH nanosheets with the thickness of ≈ 8 nm grew along with the skeleton of CNTs, leading to an open and
30 porous structure (Scheme 1: step III). The resulting single CNTs-LDH as interconnected sheet-like subunits was to form a honeycomb structure. Therefore, the agglomerated o-MWCNTs provided an orientation/confinement for LDH nanosheets formation. At the same time, a large amount of metal ions in the
35 solution deposited to form larger LDH sheets substrate (Scheme 1: step IV).

3.1.3 XRD analysis

The XRD was employed to characterize the crystal structure of the samples, as shown in Fig. 3 and Fig. S3. The o-MWCNTs
40 exhibits a broad (002) diffraction peak at 25.7° and a (101) diffraction peak at 43.17° (JCPDS No. 41-1487) [27]. It is
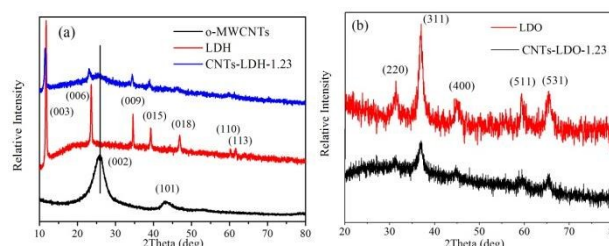

Fig.3. XRD patterns of (a) o-MWCNTs, LDH, CNTs-LDH, and (b) LDO, CNTs-LDO.

45 noteworthy that no typical diffraction peaks of CNTs are observed within the curves of CNTs-LDH-0.06, CNTs-LDH-0.31 and CNTs-LDH-0.62, the reason of which may be owing to that the o-MWCNTs were highly dispersed in the hydrotalcite structure (Fig. S3) [28]. As the amount of CNTs in the composites
50 increase, the intensity of (002) diffraction peak of o-MWCNTs became more apparent. The peaks at 11.59°, 23.22°, 34.60°, 39.07°, 46.68° and 60.26° can be indexed to (003), (006), (009), (015), (018) and (110) characteristic diffraction of hydrotalcite-like structure in both the LDH and CNTs-LDH samples.
55 However, the intensity of the CNTs-LDH nanohybrids diffraction peaks becomes relatively weak compared with that of the pristine LDH, implying that it may be a low crystallinity of nanohybrid materials and smaller LDH particle sizes in the CNTs-LDH hierarchical nano-structure [28, 29]. The sheet distances (d_{003}) of
60 LDH and CNTs-LDH are characterized as 7.63 Å and 7.71 Å, respectively. This slight increase of d_{003} may be attributed to the fact that the relatively tiny CNTs-LDH nanosheets improved strong interaction between the LDH and the o-MWCNTs, leading to the weak interaction force between the positively charged
65 hydrotalcite-like host layers and charge-balancing interlayer anions (CO_3^{2-}) [27, 30]. As is shown in Table 1, the d_{003} value of the CNTs-LDH samples gradually increases with the increase of MWCNTs contents. The presence of o-MWCNTs during the LDH growth may introduce defects into the LDH structure,
70 through modified nucleation conditions or induced curvature [29]. After calcination, the LDH structure was destructed and converted to the pre-spinel mixed metal oxides [31]. The usual spinel-like diffraction pattern is developed after calcination, which is confirmed by the corresponding (220), (311), (400),
75 (511) and (531) diffraction peaks derived form the decomposition of collapsed LDH. However, the broader

diffraction peaks of LDO may be due to the amorphous structure or dispersion of the manganese compounds in the lattice of spinel that lead to the pattern distortion. What's more, the diffraction peaks of CNTs-LDO present weaker, indicating that smaller

5 particle sizes and lower crystallinity of nanohybrid materials might be formed, which can be explained by the orientation/confinement effect of CNTs on the LDH nanosheets formation.

3.1.4 XPS analysis

10   It is well known that the catalytic activity of the obtained materials containing transition metals is associated with the oxidation state of the transition metals. Therefore, the electronic state of d-ions was studied by XPS which gave information about surface and near-surface ions. Fig.4 shows the XPS spectras of

15 Co 2p and Mn 2p of LDO and CNTs-LDO-0.62, respectively. For Co 2p, two peaks that can be assigned to $Co2p_{3/2}$ and $Co2p_{1/2}$ (known as spin orbit splitting) are observed because of the energy separation. The $15.1 \pm 0.1eV$ and $16.0 \pm 0.1eV$ of spin orbit splitting are detected in LDO and CNTs-LDO samples,

20 respectively. The former is in good agreement with the reference date of Co_3O_4, indicating the coexistence of Co (II)and Co (III) in LDO [32]. However, in the CNTs-LDO nanohybrid, cobalt is almost in divalent valence state, which may be due to that the oxidation reaction of Co (II) was inhibited by sacrificing CNTs[16].

25 The oxidation potential of Co^{2+} ($E_{Co}{}^{2+}{}_{/Co}{}^{3+}$) is -1.81 V vs SHE. The redox characteristic of MWCNTs by CV was studied as presented in Fig.8 (a). It is seen that the oxidarion peak ocuuring at -0.052 V for MWCNTs, is correlated with the redox of surface oxygen containing groups on MWCNTs. Then, the oxidation

30 potential of o-MWCNTs (E_{ox}) was 0.168V vs SHE based on E vs SHE = E vs Ag/AgCl + 0.22 V. Therefore, oxidation preferentially takes place on MWCNTs. The defect sites of o-MWCNTs are more active than the perfect ones, and carbon atoms with defects can be preferentially oxidized to oxygen-

35 containing groups during the calcining process. The difference in XPS spectra of Mn 2p between LDO and CNTs-LDO is quite modest. Fig. 4 (b) displays two peaks centered at around binding energies of 642 eV and 653 eV that can be assigned to Mn $2p_{3/2}$ and Mn $2p_{1/2}$, respectively [33]. Mn (II) or Mn (III) can be easily

40 transferred into high valence state manganese during the calcination process. Fritsh et al. [34] and Sagheer et al. [35] reported that Mn (II) and Mn (III) cations could be oxidized in the temperature range of 300-450 °C according to the following reaction:

45 $$Mn_3O_4 + \frac{2}{5}O_2 \rightarrow \frac{3}{5}Mn_5O_8 \qquad (1)$$

     High spin state of Mn (III) (d_4) was susceptible to Jahn-Teller distortion, which could further lead to the lattice instability in the LDH [32]. Therefore, Mn (III) should be oxidized to Mn (IV) to overcome the lattice instability. According to the previous

50 studies [33, 36, 37], both the Mn (III) and Mn (IV) could exist in the catalysts. This hypothesis can be proved by XPS spectra of Mn 2p3/2, in which the broad peaks of Mn 2p3/2 can be deconvolved into two peaks: the peak at 641.9-642.0 eV is assigned to Mn (III) ions and that at 643.8-644.0 eV is assigned to Mn (IV) ions [38].

55 However, the ratio of Mn (III)/Mn (IV), which reflects the "oxygen mobility " in the lattice, is different in the absence and presence of CNTs, e.g., the ratio is about 0.68 and 1.14 in LDO
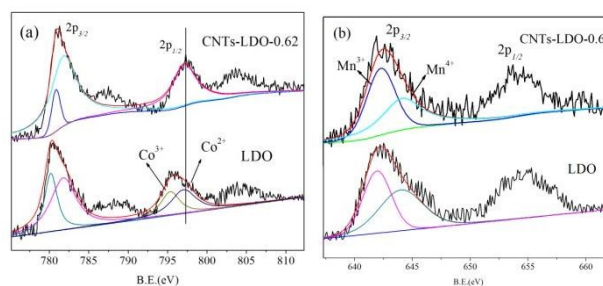
surface and CNTs-LDO surface, respectively.

60   Fig.4. XPS spectra of (a) Co 2pand (b) Mn 2p.

3.1.5 FTIR analysis

     The presence of oxygen-containing functional groups within o-MWCNTs was investigated by FT-IR spectrum (Fig. 5 (a)), in which several characteristic bands at 3423 and 1575 cm^{-1}

65 demonstrate the successful formation of hydroxyl and carboxylic groups on side walls of MWCNTs during the acid-treated process. The adsorption peaks located at 1147 and 1027 cm^{-1} are assigned to the vibration of C–O and the stretching vibration of C–O–H. Fig. 5 (b) shows the FT-IR spectra of the as-prepared

70 layered materials, in which it can be clearly seen that the broad band at around 3400 cm^{-1} is related to the stretching vibration of hydroxyl groups of inorganic layers and interlayer water, accompanied by the peak at around 1640 cm^{-1}. The strong peak at 1358 cm^{-1} is ascribed to the presence of the intercalated $CO_3{}^{2-}$

75 anions (v_3 vibration and bending modes of the interlayer anion) in the LDH and CNTs-LDH. The peaks below 800 cm^{-1} are assigned to the metal-oxygen stretching or bending modes in the LDO and CNTs-LDO. The new intense peak at 998 cm^{-1}, which corresponds attributed to the vibration of C-O in C-O-M (M =

80 Co, Mn, Al), is detected in CNTs-LDH and CNTs-LDO. It indicates the chemical bonding of oxygen bridges between LDH/LDO and CNTs [39, 40].
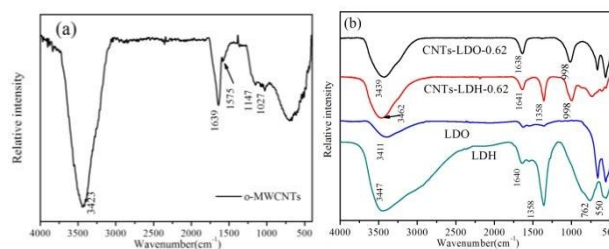

Fig.5. FTIR spectra of (a)o-MWCNTs , (b)LDO and CNTs-LDO.

85 ### 3.1.6 Raman analysis

     The structural properties of the as-synthesized samples were achieved by Raman spectra (as shown in Fig.6 and Fig. S4). KBr acted as quenching agents was added to these samples to avoid fluorescence effect. Two intense peaks at around 1324 and 1577

90 cm^{-1} can be assigned to D and G bands of carbon materials, respectively. The D band is associated with the E_{2g} in-plan vibration mode of sp^2-bonded carbon atoms in the two-dimensional hexagonal lattice of the crystalline graphite phase and shows the structural imperfections originated from the

95 attachment of oxygenated groups onto the carbon basal plane. The G band corresponds to the A_{1g} in-plane breathing vibration mode of carbon atoms with dangling bonds in the plane terminations of the disordered graphite or the presence of

amorphous carbon. The intensity ration of D band to the G band, which can provide evidence for the degree of disorder and average size of the sp^2 domains in graphitic materials, is 0.43 in o-MWCNTs, indicating that the o-MWCNTs exhibits high
5 graphitization. The Raman spectra of the as-prepared nanohybrids with different CNTs contents are shown in Fig. S4 and the graphitization of as-prepared nanohybrids are calculated and listed in Table 1. It implies that with the increasing CNTs contents in the catalysts, the I_D/I_G value, increases from 1.07 for
10 CNTs-LDH-0.06 to 1.57 for CNTs-LDH-0.62, and then decreases to 1.41 for CNTs-LDH-1.23. As mentioned above, the metal ions could be preferentially trapped by the surface defects of CNTs. Such "healing" of MWCNTs by metal compounds has been recently explained by further perturbation of outer shells with
15 reacting metal compounds, leading to decrease in the contribution of outer graphitic shell to Raman fingerprint [41, 42]. In addition, the other peaks at around 195, 488, 588, 629 and 689 cm^{-1} in the spectra of LDO and CNTs-LDO, which are related to the Raman-active modes of metal oxides, demonstrate the successful
20 integration of LDO on CNTs [42, 43]. However, the vibration intensity of carbon atoms significantly decreases after calcination. Especially, the peaks of D band and G band can't be detected in CNTs-LDO-0.06, which may be attributed to a homogeneous dispersion of LDO on the surface of MWCNTs and the strong
25 interaction between LDO and MWCNTs [44]. Moreover, the I_D/I_G value first increase till CNTs-LDO-0.62, then decrease with further increase of CNTs in the catalysts. However, it increases compared with the samples without calcination, implying the lower crystalline order of graphite phase. It may be attributed to
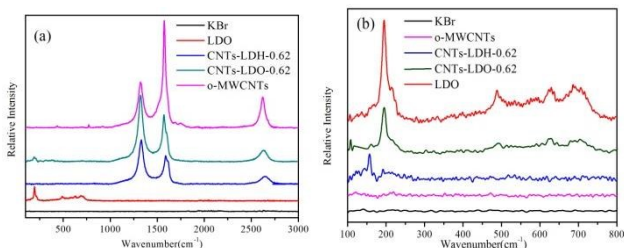30 the oxidation and loss of the carbon nanotubes during calcination.

Fig.6 Raman spectra of the as-prepared samples (a) and at short wavelength (b).

3.1.7 BET analysis

35 The nigtrogen adsorption/desorption technique was used to measure the pore structure of LDO and CNTs-LDO-X nanohybrids including specific surface area, pore volume and pore size, and the corresponding results are presented in Fig.7 and Table 1. All the samples exhibit typical IV isotherm with H3-type
40 hysteresis loops $(P/P_0 > 0.4)$, which indicate the presence of mesopores [45, 46]. Any limiting adsorption at high P/P_0 region is not exhibited for this type of hysteresis loops, which is usually ascribed to the aggregation of the particles with slit-shaped pores [28]. The amount of N_2 adsorbed on the sample near $P/P_0 = 1$
45 increased with the increase of MWCNTs contents, indicating the increase of large mesopores and macropores of the samples [47]. The hysteresis loops appearing at range of 0.4-1.0 are associated with the capillary condensation in small mesopores and accumulated pores [48]. Compared with that of CNTs-LDO
50 nanohybrids, the hysteresis loop of LDO almost disappear in the

adsorption-desorption isotherms curve, declaring that the addition of MWCNTs can increase the material's porosity. As shown in Table 1, the BET surface area increases from 141.13 to 206.48 $m^2 \cdot g^{-1}$ and the pore volume increases from 0.15 to 0.37 $m^2 \cdot g^{-1}$
55 after introducing MWCNTs into the nanohybrids. In view of the pore size distributions (Fig.7 (b)), all the samples presented mesoporous structure with a distribution in a very narrow range of 20-40 Å, which is resulted form to the aggregated pores, slit-shaped pores or inner pores of MWCNTs. The increased
60 mesoporosity at small pore sizes (20-40 Å) is considered as inner pores of MWCNTs [48], while the increased of lager pores corresponding to the aggregated pores and is possibly due to the formation of unique 3D hierarchical honeycomb nano-structure in this work. To sum up, it is reasonable to believe that the
65 introduction of MWCNTs in the composites reduce the aggregation of LDH platelets, thus leading to the exposure of more surfaces and active sites.
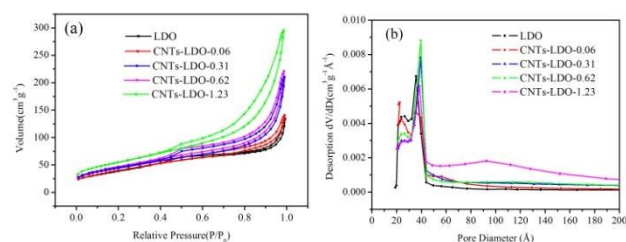

Fig.7. N_2 adsorption-desorption isotherms and pore distribution of as-
70 prepared sample.

3.1.8 CV measurements

CV measurements can be adopted to compare the electrochemical surface area and capacitance [49]. The CV curves of the o-MWCNTs and CNTs-LDO samples at O_2 atmospheres in
75 B-R buffer solution at room temperature are shown in Fig.8 (a) and Fig.8 (b). MWCNTs are potentially interesting candidates as electrode material for electrochemical capacitor due to their dominant mesoporous character, strong entanglement and perfect resiliency [50]. It can be seen from Fig. 8 (a), the o-MWCNTs
80 possess a large loop area, which is indicative of the high specific capacitance. Moreover, a oxidation peak appears at -0.052 V for o-MWCNTs, which is in correlation with the redox of surface oxygen containing groups on the MWCNTs. The loop area of CNTs-LDO increases with the increase of carbon contents, and
85 CNTs-LDO-1.23 shows the highest peak current density and the largest loop area, implying the largest electrochemical capacitance of this material. In addition, the oxidation peak value at around -0.05 V is enhanced compared with the pure LDO, which indicates the improvement of the catalytic activation of
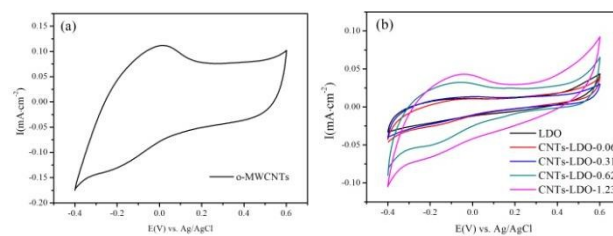90 nanohybrids.

Fig.8. CV curves for samples in pH 3 B-R buffer solution with a scan rate of 10 $mV \cdot s^{-1}$.

3.2. Catalytic oxidation of bisphenol A

Fig.9 (a) shows the preliminary tests of adsorption of BPA by o-MWCNTs, LDO and CNTs-LDO. It is found that the o-MWCNTs exhibits the highest adsorption capacity for BPA compared with that on LDO and CNTs-LDO. Moreover, the adsorption capacity of BPA decreases with the increasing amount of LDO. It is suggested that loading LDO on CNTs reduced the surface area and pore volume of o-MWCNTs (as shown in Table 1). The desorption of BPA occurs in all adsorption tests after 15 min, indicating that the adsorption of BPA is very weak. The degradation tests of BPA by different catalysts are shown in Fig.9 (b), it can be clearly seen that the BPA degradation only with PMS is relatively weak, which can be explained by the reason that the hot activation of PMS leads to the production of sulfate radicals under the neutral condition. Nevertheless, the degradation of BPA presents a gradual increase when adding PMS and o-MWNCTs simultaneously, and the degradation of BPA was higher than that of o-MWCNTs adsorption. It is suggested that o-MWCNTs could possibly activate PMS to produce sulfate radicals, and the reaction is shown as Eq. (2) below.
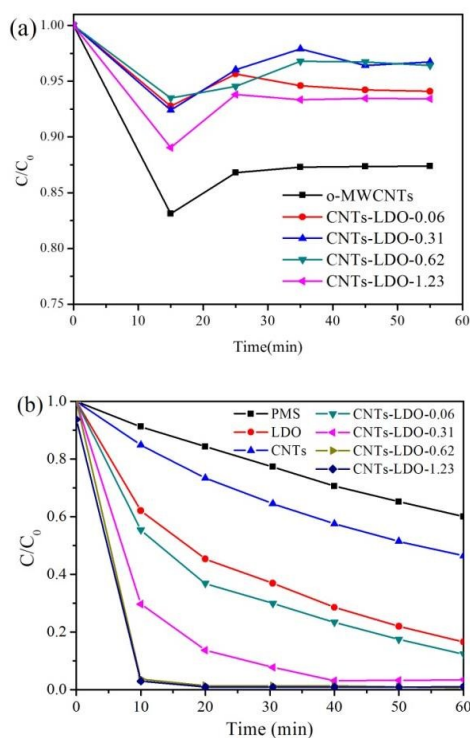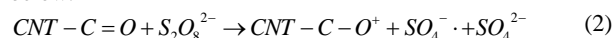
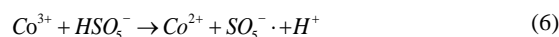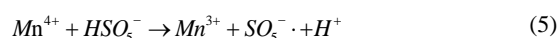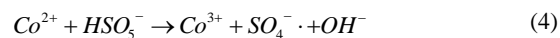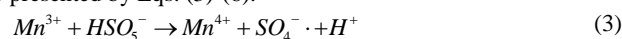$$CNT-C=O+S_2O_8^{2-} \rightarrow CNT-C-O^+ + SO_4^- \cdot + SO_4^{2-} \qquad (2)$$

Fig. 9. BPA adsorption(a) and degradation (b) on different samples. Reaction conditions: [BPA]$_0$ =20 mg·L^{-1}, sample dosage = 0.02 g·L^{-1}, T = 25°C(a), and PMS dosage = 0.15 g·L^{-1} (b)

For LDO/PMS system, 100% BPA degradation could be achieved after 80 min. The activation of PMS by LDO could be presented by Eqs. (3)-(6).

$$Mn^{3+} + HSO_5^- \rightarrow Mn^{4+} + SO_4^- \cdot + H^+ \qquad (3)$$

$$Co^{2+} + HSO_5^- \rightarrow Co^{3+} + SO_4^- \cdot + OH^- \qquad (4)$$

$$Mn^{4+} + HSO_5^- \rightarrow Mn^{3+} + SO_5^- \cdot + H^+ \qquad (5)$$

$$Co^{3+} + HSO_5^- \rightarrow Co^{2+} + SO_5^- \cdot + H^+ \qquad (6)$$

Note that the catalytic performance in BPA oxidation was significantly improved with the addition of CNTs-LDO nanohybrids. Moreover, the degradation efficiency increased with the increase of CNTs contents. Typically, 20 mg·L^{-1} of BPA was completely degraded within 10 min by 0.02 g·L^{-1} of CNTs-LDO-0.62 and 0.15 g·L^{-1} of PMS.

The BPA degradation in the presence of LDO or CNTs-LDO was correlated with the TOC removals as shown in Fig. S5. About 25% and 45% of TOC was removed after 80 min in LDO/PMS system and CNTs-LDO-0.62/PMS system, respectively. It indicates that the introduction of CNTs into the catalysts is in favor of the BPA degradation and the removal of TOC.

3.3. Stability of CNTs-LDO in miltiple runs

The recycling ability of CNTs-LDO-0.62 nanohybrid was determined by adding recycled catalyst from previous runs into fresh BPA solutions for degradation under the same reaction conditions, as shown in Fig.10. The activity of catalyst has not changed in the three cycles. The concentration of dissolved Co and Mn ions from LDO was measured by AAS. The Mn leached from all samples was < 0.005 mg·L^{-1}, which was below the detection limit. As shown in Fig. 11, trace amounts of leaching Co were detected and increased with the increase of CNTs contents, which indicates the stability of catalysts reduced after adding CNTs.
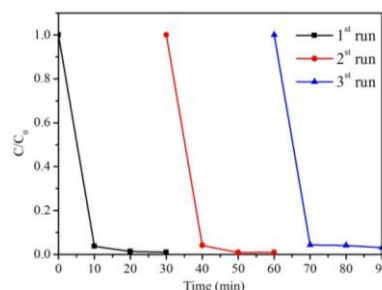

Fig.10. Degradation of BPA and dissolution of Co and Mn from catalyst in consecutive runs using the recycled CNTs-LDO-0.62 at neutral pH.Reaction conditions: [BPA]$_0$ =20 mg·L^{-1}, catalyst dosage = 0.02 g·L^{-1}, T = 25 ^{o}C, and PMS dosage = 0.15 g·L^{-1}.
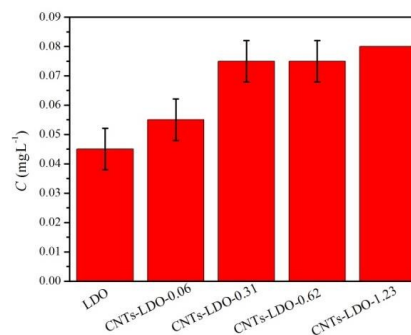

Fig. 11. The leaching amount of Co after degradation.

3.4. Role of MWCNTs in CNTs-LDO nanohybrids incatalytic activation of PMS

In this work, the transformation of morphology, structure and composition of the mixture metal oxides was observed in the presence of MWCNTs. For example, the morphology of mixed metal oxides was transformed from stacked 2D hexagonal plate to 3D hierarchical honeycomb because of the orientation/confinement of MWCNTs; the particle size decreased and the surface area increased with the addition of MWCNTs; the transition metal was hard to oxidize during calcination which might be due to the reduction of MWCNTs.

In previous study, Anipsitakis et al.[51] studied the heterogenous activation of PMS by using cobalt oxides, CoO and Co_3O_4, and found that only Co_3O_4 activated PMS heterogeneously. Therefore, in this work, Co existed in CNTs-LDO at +2 valence state is not the reason of much higher catalytic activity. In terms of the morphology and structure of the nanohybrids, the CNTs-LDH was fabricated with a 3D hierarchical honeycomb structure, which greatly reduced the aggregation of LDH platelets and MWCNTs and thus leading to the exposure of more surface and activity sites. Besides, the oxidized and lost part of the carbon nanotubes occurred during the calcination, could lead to the lower crystalline order of graphite phase and higher MWCNTs defect densities according to the Raman analysis. Song et al.[12] reported that MWCNTs with different defect densities had been used directly as catalyst for the activation of H_2O_2. The results showed that the performance of the catalyst was improved with the increasing defect densities of MWCNTs, and active oxygen was generated by H_2O_2 decomposition on the defect of MWCNTs with dangling incomplete bonding. Therefore, MWCNTs defects generated by calcination might increase PMS activation for the production of sulfate radicals in this work.

Conclusion

In conclusion, the results obtained herein provide clear evidence that the CNTs-LDH and CNTs-LDO nanohybrids with a 3D hierarchical honeycomb structure are formed by the deposition of CNTs-LDH nanosheets on LDH sheets substrates. The transformations of surface morphology, structure and composition of the as-prepared materials in the presence or absence of MWCNTs are depicted in this work. The catalytic performance of the clacined products can be significantly enhanced with the increase of o-MWCNTs contents in the hybrids. The unique 3D hierarchical honeycomb structure and MWCNTs defects play important roles in the catalytic activation of PMS for BPA degradation. Typically, 20 mg·L^{-1} of BPA was completely degraded by 0.02 g·L^{-1} of CNTs-LDO-0.62 and 0.15 g·L^{-1} of PMS within 10 min. Therefore, the preliminary results confirmed that this new kind of heterogeneous catalysts with a 3D hierarchical honeycomb structure could be applied in the effective BPA degradation.

Acknowledgments

Notes and references

a College of Environment and Energy, South China University of Technology, Guangzhou 510006, P.R. China
b The Key Lab of Pollution Control and Ecosystem Restoration in Industry Clusters, Ministry of Education, Guangzhou 510006, P.R. China
c The Key Laboratory of Environmental Protection and Eco-Remediation of Guangdong Regular Higher Education Institutions, P.R. China

† Electronic Supplementary Information (ESI) available: TEM images of o-MWCNTs and SEM images of CNTs-LDO-0.62. EDS mapping of CNTs-LDO-1.23, LDO, CNTs-LDH-1.23 and LDH. XRD patterns of CNTs-LDH and CNTs-LDO. Raman spectra of (a) CNTs-LDH and (b) CNTs-LDO. TOC removal on different catalytic. The adsorption of Co and Mn during the preparation of samples. See the file designation of Electronic Supplementary Information (reviewers will see).

1. M. Zhao, Q. Zhang, J. Huang and F. Wei, Adv. Funct. Mater., 2012, 22, 675-694.
2. Y. Yao, Z. Yang, H. Sun and S. Wang, Ind. Eng. Chem. Res., 2012, 51, 14958-14965.
3. Y. Yao, Y. Cai, F. Lu, F. Wei, X. Wang and S. Wang, J. Hazard. Mater., 2014, 270, 61-70.
4. R. Xu, H. Bi, G. He, J. Zhu and H. Chen, Mater. Res. Bull., 2014, 57, 190-196.
5. Z. Huang, P. Wu, B. Gong, Y. Fang and N. Zhu, Journal of Materials Chemistry A, 2014, 2, 5534-5540.
6. E. Saputra, S. Muhammad, H. Sun and S. Wang, RSC Advances, 2013, 3, 21905-21910.
7. P. Shi, R. Su, S. Zhu, M. Zhu, D. Li and S. Xu, J. Hazard. Mater., 2012, 229, 331-339.
8. S. Liu, W. Peng, H. Sun and S. Wang, Nanoscale, 2014, 6, 766-771.
9. H. Sun, C. Kwan, A. Suvorova, H. M. Ang, M. O. Tadé and S. Wang, Applied Catalysis B: Environmental, 2014, 154, 134-141.
10. W. Chen, D. Zhu, S. Zheng and W. Chen, Environ. Sci. Technol., 2014, 48, 3856-3863.
11. S. Jiang and S. Song, Applied Catalysis B: Environmental, 2013, 140, 1-8.
12. S. Song, H. Yang, R. Rao, H. Liu and A. Zhang, Catalysis Communications, 2010, 11, 783-787.
13. W. Peng, S. Liu, H. Sun, Y. Yao, L. Zhi and S. Wang, Journal of Materials Chemistry A, 2013, 1, 5854-5859.
14. M. Grzelczak, J. Vermant, E. M. Furst and L. M. Liz-Marzán, ACS Nano, 2010, 4, 3591-3605.
15. W. Zhang, B. Xu and L. Jiang, J. Mater. Chem., 2010, 20, 6383-6391.
16. S. Song, S. Jiang, R. Rao, H. Yang and A. Zhang, Applied Catalysis A: General, 2011, 401, 215-219.
17. T. Dang, A. N. Banerjee, S. W. Joo and B. Min, Ind. Eng. Chem. Res., 2014.
18. S. Jiang and S. Song, Applied Catalysis B: Environmental, 2013, 140, 1-8.
19. Zhao, J. Masa, W. Xia, A. Maljusch, M. Willinger, G. Clavel, K. Xie, R. Schlögl, W. Schuhmann and M. Muhler, J. Am. Chem. Soc., 2014, 136, 7551-7554.
20. X. Zhang, J. Wang, R. Li, Q. Dai, R. Gao, Q. Liu and M. Zhang, Ind. Eng. Chem. Res., 2013, 52, 10152-10159.
21. L. Xu and J. Wang, Environ. Sci. Technol., 2012, 46, 10145-10153.
22. E. Saputra, S. Muhammad, H. Sun, H. M. Ang, M. O. Tadé and S. Wang, Environ. Sci. Technol., 2013, 47, 5882-5887.
23. H. Liang, H. Sun, A. Patel, P. Shukla, Z. H. Zhu and S. Wang, Applied Catalysis B: Environmental, 2012, 127, 330-335.
24. S. He, Z. An, M. Wei, D.G. Evans, X. Duan, Chem Commun 49 (2013) 5912-5920.
25. P.J. Sideris, U.G. Nielsen, Z. Gan, C.P. Grey, Science 321 (2008) 113-117.
26. Q. Liao, J. Sun and L. Gao, Colloids and Surfaces A: Physicochemical and Engineering Aspects, 2009, 345, 95-100.
27. J. Yang, C. Yu, X. Fan, Z. Ling, J. Qiu and Y. Gogotsi, Journal of Materials Chemistry A, 2013, 1, 1963-1968.

28. W. Yang, Z. Gao, J. Wang, J. Ma, M. Zhang and L. Liu, ACS Applied Materials & Interfaces, 2013, 5, 5443-5454.

29. Garcia-Gallastegui, D. Iruretagoyena, M. Mokhtar, A. M. Asiri, S. N. Basahel, S. A. Al-Thabaiti, A. O. Alyoubi, D. Chadwick and M. S. P. Shaffer, J. Mater. Chem., 2012, 22, 13932-13940.

30. H. Wang, X. Xiang and F. Li, J. Mater. Chem., 2010, 20, 3944-3952.

31. F. Kovanda, T. Rojka, J. Dobešová, V. Machovič, P. Bezdička, L. Obalová, K. Jirátová and T. Grygar, J. Solid State Chem., 2006, 179, 812-823.

32. N. V. Kosova, E. T. Devyatkina and V. V. Kaichev, J. Power Sources, 2007, 174, 735-740.

33. Y. Zhang, Z. Qin, G. Wang, H. Zhu, M. Dong, S. Li, Z. Wu, Z. Li, Z. Wu, J. Zhang, T. Hu, W. Fan and J. Wang, Applied Catalysis B: Environmental, 2013, 129, 172-181.

34. S. Fritsch, J. Sarrias, A. Rousset and G. U. Kulkarni, Mater. Res. Bull., 1998, 33, 1185-1194.

35. F. A. Al Sagheer, M. A. Hasan, L. Pasupulety and M. I. Zaki, 1999, 18, 209-211.

36. J. Lamonier, A. Boutoundou, C. Gennequin, M. Pérez-Zurita, S. Siffert and A. Aboukais, 2007, 118, 165-172.

37. L. Obalová, G. Maniak, K. Karásková, F. Kovanda and A. Kotarba, Catalysis Communications, 2011, 12, 1055-1058.

38. H. Li, G. Lu, Q. Dai, Y. Wang, Y. Guo and Y. Guo, Applied Catalysis B: Environmental, 2011, 102, 475-483.

39. H. Fu, Z. Du, W. Zou, H. Li and C. Zhang, Carbon, 2013, 65, 112-123.

40. J. Zhou, H. Song, L. Ma and X. Chen, RSC Advances, 2011, 1, 782-791.

41. M. Cargnello, M. Grzelczak, B. Rodríguez-González, Z. Syrgiannis, K. Bakhmutsky, V. La Parola, L. M. Liz-Marzán, R. J. Gorte, M. Prato and P. Fornasiero, J. Am. Chem. Soc., 2012, 134, 11760-11766.

42. R. Nie, J. Shi, W. Du, W. Ning, Z. Hou and F. Xiao, Journal of Materials Chemistry A, 2013, 1, 9037-9045.

43. J. Qu, L. Shi, C. He, F. Gao, B. Li, Q. Zhou, H. Hu, G. Shao, X. Wang and J. Qiu, Carbon, 2014, 66, 485-492.

44. R. Nie, J. Shi, W. Du, W. Ning, Z. Hou and F. Xiao, Journal of Materials Chemistry A, 2013, 1, 9037-9045.

45. C. Yu, J. Yang, C. Zhao, X. Fan, G. Wang and J. Qiu, Nanoscale, 2014, 6, 3097-3104.

46. J. Zhao, J. Chen, S. Xu, M. Shao, Q. Zhang, F. Wei, J. Ma, M. Wei, D. G. Evans and X. Duan, Adv. Funct. Mater., 2014, 24, 2938-2946.

47. Q. Ma, D. Wang, M. Wu, T. Zhao, Y. Yoneyama and N. Tsubaki, Fuel, 2013, 108, 430-438.

48. Y. QH., B. S., W. MZ., C. HM. and H. PX., 2001, 345, 18-24.

49. B. Li, J. Qiao, D. Yang, J. Zheng, J. Ma, J. Zhang and H. Wang, Electrochim. Acta, 2009, 54, 5614-5620.

50. K. Jurewicz, K. Babeł, R. Pietrzak, S. Delpeux and H. Wachowska, Carbon, 2006, 44, 2368-2375.

51. G. P. Anipsitakis, E. Stathatos and D. D. Dionysiou, The Journal of Physical Chemistry B, 2005, 109, 13052-13055.

RSC Advances Accepted Manuscript